Monthly Notices of the ROYAL ASTRONOMICAL SOCIETY

MNRAS **457,** 1739–1752 (2016) doi:10.1093/mnras/stw022

# The most luminous H$\alpha$ emitters at $z \sim 0.8$–2.23 from HiZELS: evolution of AGN and star-forming galaxies[⋆]

David Sobral,[1,2,3,4]†‡ Saul A. Kohn,[3,5] Philip N. Best,[6] Ian Smail,[7]
Chris M. Harrison,[7] John Stott,[7,8] João Calhau[1,2,4] and Jorryt Matthee[3]

[1] *Instituto de Astrofísica e Ciências do Espaço, Universidade de Lisboa, OAL, Tapada da Ajuda, P-1349-018 Lisboa, Portugal*
[2] *Departamento de Física, Faculdade de Ciências, Universidade de Lisboa, Edifício C8, Campo Grande, P-1749-016 Lisbon, Portugal*
[3] *Leiden Observatory, Leiden University, P.O. Box 9513, NL-2300 RA Leiden, the Netherlands*
[4] *Department of Physics, Lancaster University, Lancaster LA1 4YB, UK*
[5] *Department of Physics and Astronomy, University of Pennsylvania, Philadelphia, PA 19104, USA*
[6] *SUPA, Institute for Astronomy, Royal Observatory, Blackford Hill, Edinburgh EH9 3HJ, UK*
[7] *Centre for Extragalactic Astronomy, Department of Physics, Durham University, South Road, Durham DH1 3LE, UK*
[8] *Sub-department of Astrophysics, Department of Physics, University of Oxford, Denys Wilkinson Bld., Keble Road, Oxford OX1 3RH, UK*

Accepted 2016 January 4. Received 2016 January 4; in original form 2015 October 10

## ABSTRACT

We use new near-infrared spectroscopic observations to investigate the nature and evolution of the most luminous H$\alpha$ emitters at $z \sim 0.8$–2.23, which evolve strongly in number density over this period, and compare them to more typical H$\alpha$ emitters. We study 59 luminous H$\alpha$ emitters with $L_{\mathrm{H}\alpha} > L^{*}_{\mathrm{H}\alpha}$, roughly equally split per redshift slice at $z \sim 0.8$, 1.47 and 2.23 from the HiZELS and CF-HiZELS surveys. We find that, overall, $30 \pm 8$ per cent are active galactic nuclei [AGNs; $80 \pm 30$ per cent of these AGNs are broad-line AGNs, BL-AGNs], and we find little to no evolution in the AGN fraction with redshift, within the errors. However, the AGN fraction increases strongly with H$\alpha$ luminosity and correlates best with $L_{\mathrm{H}\alpha}/L^{*}_{\mathrm{H}\alpha}(z)$. While $L_{\mathrm{H}\alpha} \leq L^{*}_{\mathrm{H}\alpha}(z)$ H$\alpha$ emitters are largely dominated by star-forming galaxies (>80 per cent), the most luminous H$\alpha$ emitters ($L_{\mathrm{H}\alpha} > 10L^{*}_{\mathrm{H}\alpha}(z)$) at any cosmic time are essentially all BL-AGN. Using our AGN-decontaminated sample of luminous star-forming galaxies, and integrating down to a fixed H$\alpha$ luminosity, we find a factor of ∼1300 evolution in the star formation rate density from $z = 0$ to 2.23. This is much stronger than the evolution from typical H$\alpha$ star-forming galaxies and in line with the evolution seen for constant luminosity cuts used to select 'ultraluminous' infrared galaxies and/or sub-millimetre galaxies. By taking into account the evolution in the typical H$\alpha$ luminosity, we show that the most strongly star-forming H$\alpha$-selected galaxies at any epoch ($L_{\mathrm{H}\alpha} > L^{*}_{\mathrm{H}\alpha}(z)$) contribute the same fractional amount of ≈15 per cent to the total star formation rate density, at least up to $z = 2.23$.

**Key words:** galaxies: evolution – galaxies: high-redshift – cosmology: observations.

## 1 INTRODUCTION

Surveys show that the peak of the star formation history (e.g. Lilly et al. 1996; Hopkins & Beacom 2006; Reddy et al. 2008; Sobral et al. 2013a; Swinbank et al. 2014) and active galactic nuclei (AGNs; e.g. Wolf et al. 2003; Ackermann et al. 2011) activity lies within the redshift interval $z = 1$–3, although there are suggestions that the peak of star formation activity may occur earlier ($z \sim 2$–2.5; e.g. Karim et al. 2011; Sobral et al. 2013a) than that of AGN ($z \sim 1$–2; e.g. Aird et al. 2010; Ueda et al. 2014). There is also evidence that the strong evolution in star formation activity has happened for galaxies at all masses (e.g. Sobral et al. 2014; Drake et al. 2015) and in all environments (e.g. Koyama et al. 2013).

H$\alpha$ is an excellent instantaneous tracer of star formation activity (e.g. Kennicutt 1998). By using the narrow-band technique (see also grism surveys; e.g. Colbert et al. 2013) on very wide field near-infrared (NIR) detectors, H$\alpha$ can be used to conduct very large, sensitive surveys up to $z \sim 2.5$ (e.g. Kurk et al. 2004; Geach et al. 2008; Lee et al. 2012; Koyama et al. 2013; Sobral et al. 2013a; Stroe & Sobral 2015). Measuring the evolution of the H$\alpha$ luminosity

---

[⋆] This research is based on data gathered at the ESO New Technology Telescope under programmes 087.A-0337 and 089.A-0965, Telescopio Nazionale Galileo, with time awarded through OPTICON programmes 2011A/026 and 2012A020 and the William Herschel Telescope under programme W12BN007.
† VENI/FCT IF Fellow.
‡ E-mail: sobral@strw.leidenuniv.nl

Published by Oxford University Press on behalf of the Royal Astronomical Society

function (LF) is one of the main goals of High-$z$ Emission Line Survey (HiZELS; Geach et al. 2008; Sobral et al. 2009, 2012, 2013a; Best et al. 2013). Using the H$\alpha$ emission line as a star formation indicator allows the use of the same robust, well-calibrated and sensitive indicator over ∼11 Gyr of cosmic time. Several studies have now explored this unique potential, both from the ground and from space, to unveil the evolution of morphologies, dynamics and metallicities of star-forming galaxies (SFGs; e.g. Fumagalli et al. 2012; Livermore et al. 2012; Swinbank et al. 2012; Colbert et al. 2013; Domínguez et al. 2013; Koyama et al. 2013; Sobral et al. 2013b, 2015; Stott et al. 2013a,b; Tadaki et al. 2013; An et al. 2014; Darvish et al. 2014; Price et al. 2014).

These studies show that in the last 11 Gyr since $z \sim 2.5$, the space density of luminous H$\alpha$ emitters ($L_{\mathrm{H}\alpha} > 10^{42}$ erg s$^{-1}$) has dropped by several orders of magnitude (e.g. Geach et al. 2008; Lee et al. 2012; Colbert et al. 2013; Sobral et al. 2013a, 2015; Stroe & Sobral 2015). Sobral et al. (2013a) find that the strong evolution in the H$\alpha$ LF is best described by the evolution of the typical H$\alpha$ luminosity ($L^*_{\mathrm{H}\alpha}$) with redshift (although $\Phi^*$ is also shown to evolve). In practice, studies find an order-of-magnitude increase in the characteristic $L^*_{\mathrm{H}\alpha}$ or the knee of the star formation rate function, SFR$^*$ from $z \sim 0$ to $z \sim 2.2$ (Geach et al. 2008; Sobral et al. 2009, 2013a, 2014; Hayes, Schaerer & Östlin 2010; Lee et al. 2012). Similar evolution is found for other nebular lines such as [O II] and H$\beta$+[O III] (e.g. Khostovan et al. 2015). Interestingly, the most significant changes within the H$\alpha$ population at the peak of star formation history seem to be driven by or linked to this strong luminosity evolution of H$\alpha$ emitters (cf. Sobral et al. 2009, 2012, 2013a). In fact, when one normalizes H$\alpha$ luminosities by $L^*_{\mathrm{H}\alpha}(z)$, taking into account its evolution with redshift, many of the relations with luminosity, which would be found to evolve with redshift, fall back, to first order, to an almost-invariant relation that does not depend on cosmic time (see e.g. clustering and dust extinction studies; Sobral et al. 2010, 2012; Stott et al. 2013b). Clustering studies have shown that $\sim L^*_{\mathrm{H}\alpha}$ galaxies seem to have been hosted by Milky Way-mass haloes ($\sim 10^{12}$ M$_{\odot}$) at least since $z \sim 2.2$ (Sobral et al. 2010; Geach et al. 2012; Stroe & Sobral 2015), while $\gg L^*_{\mathrm{H}\alpha}$ emitters seem to reside in $10^{13}$ M$_{\odot}$ or higher mass dark matter haloes. This may be important if we are to understand the processes that may quench the most massive galaxies. It is therefore essential to understand the nature of such luminous H$\alpha$ sources and whether they host AGNs.

While there are many ways to identify AGNs within a sample of emission line galaxies, including the use of X-rays, radio and mid-infrared (e.g. Lacy et al. 2004, 2007; Garn et al. 2010; Stern et al. 2012; Brandt & Alexander 2015), rest-frame optical spectroscopy is still one of the most robust ways to identify AGN. The identification of AGN is particularly simple and straightforward in the presence of luminous broad Balmer lines [typically full width at half-maximum (FWHM) well in excess of 1000 km s$^{-1}$], which indicate AGN. For narrow-line emission line sources, well-chosen emission line ratios are the most robust way to identify any AGN. Baldwin, Phillips & Terlevich (1981) were among the first to recognize the importance of emission line ratios for distinguishing SFGs from AGNs. Their diagnostic (the 'BPT diagram') was based on using the relative line intensities in order to reveal the dominant excitation mechanism that operates upon the line-emitting gas: photoionization by OB stars (in SFGs) or by a power-law continuum (AGNs). More recently, Kewley et al. (2013) argue that the BPT calibration needs to be adjusted to account for the redshift evolution in the interstellar medium conditions and radiation field, which is observed in galaxies across cosmic time.

Many studies have sought to use the BPT and similar emission line diagnostics to reveal the nature of low- to intermediate-redshift galaxies (e.g. Brinchmann et al. 2004; Obrić et al. 2006; LaMassa et al. 2012). Smolčić et al. (2006) found a tight correlation between the rest-frame colours of emission line galaxies and their position on the BPT diagram. Other studies have used spectral energy distribution template fitting to separate AGNs and SFGs within large samples (e.g. Fu et al. 2010; Kirkpatrick et al. 2012) by exploring *Spitzer* spectroscopy and imaging, combined with deep *Herschel* data. Such studies find evidence for a co-evolution scenario (at least since $z \sim 1$), in which a period of intense accretion on to the central black hole (BH) of a galaxy may coincide with starburst episode, but over different time-scales (e.g. Fu et al. 2010). Other studies have focused on Lyman-break galaxies (e.g. Schenker et al. 2013) and X-ray-selected sources (e.g. Trump et al. 2013). Indeed, with instruments such as KMOS (for early science results, see e.g. Sharples et al. 2006; Sobral et al. 2013b; Stott et al. 2014; Wuyts et al. 2014) and MOSFIRE (e.g. McLean et al. 2008; Kriek et al. 2014) now fully operational, many more similar and larger studies will be possible, but those will be mostly focusing on $\leq L^*_{\mathrm{H}\alpha}$ galaxies. Despite the interest in and importance of highly luminous emitters in the high-redshift H$\alpha$ LF, little is known about them due to the difficulty of consistently selecting targets and following them up spectroscopically.

In this paper, we present NIR spectroscopic observations, and subsequent analyses, of the most luminous H$\alpha$ emitting galaxies in HiZELS and CF-HIZELS (Sobral et al. 2013a, 2015): $> L^*_{\mathrm{H}\alpha}$ H$\alpha$ emitters. Our goal is to unveil the nature of such luminous H$\alpha$ emitters and to investigate their potential evolution across cosmic time. The paper is organized as follows. In Section 2, we describe the sample, observations and data reduction. Section 3 presents the redshift distributions, explains the spectral line measurements and presents the analysis. We present the results and discussion in Section 4, and unveil the nature and evolution of luminous H$\alpha$ emitters across cosmic time. We also present an AGN-decontaminated SFR history of the Universe over the past ∼11 Gyr. We summarize our findings and conclude in Section 5. We use AB magnitudes, a Chabrier initial mass function and assume a cosmology with $H_0 = 70$ km s$^{-1}$ Mpc$^{-1}$, $\Omega_{\mathrm{M}} = 0.3$ and $\Omega_{\Lambda} = 0.7$.

## 2 OBSERVATIONS AND DATA REDUCTION

### 2.1 Sample selection: HiZELS H$\alpha$ luminous emitters

We selected H$\alpha$ luminous sources likely to be at $z = 0.84$, 1.47 and 2.23 from HiZELS (Sobral et al. 2009, 2012, 2013a; Best et al. 2013) and $z = 0.81$ from the CF-HiZELS survey (Sobral et al. 2013b, 2015; Matthee et al. 2014). HiZELS used the Wide Field Camera on the United Kingdom Infrared Telescope, to select emission line galaxies at various redshifts using specially designed narrow-band filters in the $J$ (NB$_J$) and $H$ bands (NB$_H$), along with the H$_2$S(1) filter in the $K$ band (NB$_K$). HiZELS surveyed ∼0.8 deg$^2$ contiguous regions in UKIDSS (Lawrence et al. 2012) UDS and SA22 fields, the Boötes field (e.g. Brand et al. 2006) and ∼1.6 deg$^2$ in the COSMOS field (Scoville et al. 2007) field. CF-HiZELS used WIRCAM on Canada–France–Hawaii Telescope to obtain an ∼10 deg$^2$ narrow-band survey in the $J$ band over the SA22 field. The addition of the $z = 0.81$ CF-HiZELS sample allows us to select luminous emitters at $z \sim 0.8$ by probing a volume much more comparable to that of $z \sim 1.47$ and $z \sim 2.23$ HiZELS studies. For the rest of the paper, we will refer to the sample at $z = 0.81$ and 0.84 as our $z \sim 0.8$ sample. For SA22 and Boötes (where photometric data do not

**Table 1.** A summary of the fields used in this study, the area covered with narrow-band imaging and the number of luminous Hα emitters targeted in each of the fields.

| Narrow-band ($z$, redshift) | Field | Area (deg$^2$) | No. of targets |
|---|---|---|---|
| NB$_J$ | COSMOS | 0.8 | 7 |
| ($z \sim 0.8$) | SA22 | 10 | 11 |
| | UDS | 0.6 | 5 |
| NB$_H$ | Boötes | 0.8 | 6 |
| ($z \sim 1.47$) | COSMOS | 1.6 | 7 |
| | SA22 | 0.8 | 10 |
| | UDS | 0.8 | 12 |
| NB$_K$ | COSMOS | 1.6 | 9 |
| ($z \sim 2.23$) | SA22 | 0.8 | 6 |
| | UDS | 0.8 | 6 |

reach the excellence level of COSMOS and UDS), and in order to assure a high completeness, we opt to follow up all of the brightest line emitters selected from each of the narrow-band filters. For UDS and COSMOS, we use the sample presented by Sobral et al. (2013a). Briefly, the sample of Hα emitters is selected (isolating Hα emitters from other higher and lower redshift line emitters) using (i) spectroscopic redshift confirmation with other emission lines, (ii) photometric redshifts and (iii) colour–colour selections to exclude non-Hα emitters. We refer the reader to Sobral et al. (2013a) for further details.

Our choice of flux cuts was motivated by the need to consistently trace luminous Hα emitters across redshifts. To this end, we took into account the increase in the knee of Hα LF ($L^*_{\mathrm{H}\alpha}$) with redshift (Sobral et al. 2013a):[1]

$$\log L^*_{\mathrm{H}\alpha} = 0.45z + 41.47. \tag{1}$$

We then selected sources which had luminosities corresponding to $\geq 1.0\ L^*_{\mathrm{H}\alpha}(z)$ and reaching up to $\sim 50\ L^*_{\mathrm{H}\alpha}(z)$, with number densities in the range $10^{-3.2}$–$10^{-6}$ Mpc$^{-3}$. Our luminosity limits roughly correspond to (observed) fluxes greater than ∼3, ∼2 and $\sim 1.5 \times 10^{-16}$ erg s$^{-1}$ cm$^{-2}$ for $z \sim 0.8$, 1.47 and 2.23, respectively. Our targets are distributed across the HiZELS fields: the UKIDSS UDS and SA22 fields, the COSMOS field and the Boötes field (see Table 1). For full details on the catalogues, see Sobral et al. (2013a, 2015).

### 2.1.1 NB$_J$ sample (Hα $z \sim 0.8$)

We selected 23 candidate line emitters with narrow-band $J$ (NB$_J$) estimated line fluxes higher than $3.0 \times 10^{-16}$ erg s$^{-1}$ cm$^{-2}$ (average flux of $7.3 \times 10^{-16}$ erg s$^{-1}$ cm$^{-2}$): 11 from SA22, 5 from UDS and 7 from the COSMOS field.

### 2.1.2 NB$_H$ sample (Hα $z = 1.47$)

We selected 35 candidate line emitters (likely Hα emitters at $z = 1.47$) with the highest narrow-band (NB$_H$) fluxes, $>2.0 \times 10^{-16}$ erg s$^{-1}$ cm$^{-2}$ (average flux of $1.1 \times 10^{-15}$ erg s$^{-1}$ cm$^{-2}$). From these, 12 sources are from the UDS field, 10 from SA22, 7 sources are found in the COSMOS field and the remaining 6 sources are from the Boötes field (without a colour–colour or photometric redshift pre-selection, thus more likely to have contaminants).

### 2.1.3 NB$_K$ sample (Hα $z = 2.23$)

For our sample at $z = 2.23$, we select a total of 21 sources: 9 sources from COSMOS, 6 from UDS and 6 sources from SA22 (without a colour–colour or photometric redshift pre-selection). We select them for being NB$_K$ emitters with NB estimated line fluxes $>1.5 \times 10^{-16}$ erg s$^{-1}$ cm$^{-2}$ (average flux of $5.7 \times 10^{-16}$ erg s$^{-1}$ cm$^{-2}$).

### 2.1.4 Comparison sample: NB$_J$ and NB$_H$ follow-up with FMOS

In order to explore a wider parameter space, and to be able to compare our luminous Hα emitters with those which are much more typical at their redshifts, we use a comparable spectroscopic sample of lower luminosity Hα emitters at $z = 0.84$ and 1.47 from Stott et al. (2013b), observed with FMOS on the 8 m Subaru telescope. Because the sample is the result of follow-up of candidate Hα emitters from exactly the same parent samples as we are using here, it is an ideal sample to compare our results with more 'typical' sources.

## 2.2 Spectroscopic observations

We observed our samples of luminous line emitter candidates in the NIR, in order to probe the rest-frame optical and recover, with a single spectrum, Hβ, [O III], Hα and [N II] – see Fig. 1. In order to achieve our goals, we used NTT/SofI (New Technology Telescope/Son of ISAAC), WHT/LIRIS (William Herschel Telescope/Long-slit Intermediate Resolution Infrared Spectrograph) and TNG/NICS (Telescopio Nazionale Galileo/Near-Infrared Camera and Spectrometer; see Table 2). The details of our observations using each instrument are discussed next, while Fig. 1 shows examples of spectra gathered using the different instruments and at the different redshifts. Typical total exposure times per source were very modest: ∼3 ks pixel$^{-1}$, but ranged from 1.8 ks pixel$^{-1}$ for the brightest sources to 8 ks pixel$^{-1}$ for the sources with the faintest observed flux.

### 2.2.1 NTT/SofI: NB$_J$, NB$_H$ and NB$_K$ samples

We used SofI (Moorwood, Cuby & Lidman 1998) on the European Southern Observatory (ESO) NTT in La Silla over 2011 September 23–25 and 2012 September 18–21 (see Table 2). We obtained spectra of sources selected from SA22 and UDS. During the 2011 run, we used the 1 arcsec slit and the blue grism with $R \sim 1000$ (9500–16 400 Å, corresponding to the rest-frame range 3900–6700 Å for sources at $z \sim 1.47$), which allowed simultaneous $YJH$ coverage. In 2012 the 1 arcsec slit and the blue grism (corresponding to a rest-frame range 5300–9000 Å for objects at $z \sim 0.8$), and the 1 arcsec slit with the red grism with $R \sim 1000$ (15 300–25 200 Å, corresponding to rest-frame range 4700–7800 Å for objects at $z \sim 2.23$) were used. All observations were conducted under clear conditions.

Individual exposures were 200 s in the instrument's non-destructive mode. We applied offsets along the slit for different exposures of the same target (∼30 arcsec on average), which were

---

[1] Note that the equation presented in Sobral et al. (2013a) was derived assuming $A_{\mathrm{H}\alpha} = 1$ mag, and thus to correct back to the observed $L^*$ one needs to subtract 0.4 dex. The version presented here is for observed Hα luminosities.

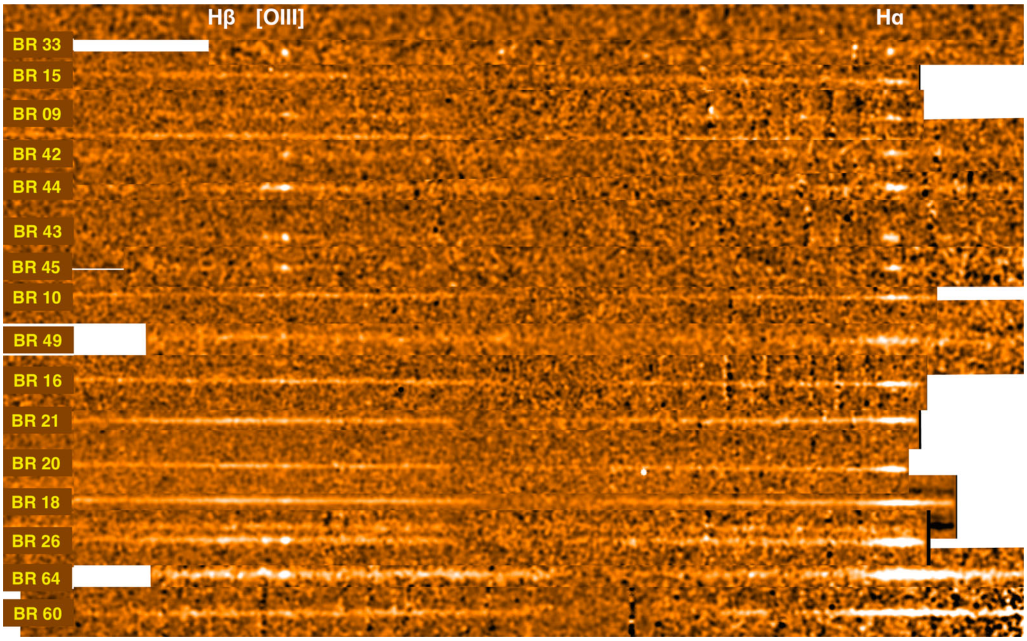

**Figure 1.** Example 2D reduced spectra from WHT/LIRIS (top and bottom sources; BR-33 and BR-60) and NTT/SofI (remaining sources) at $z = 0.8$, 1.47 and 2.23. Note that white spaces/regions are due to the slightly different (rest-frame) spectral coverage. We show examples which, from top to bottom, represent an increase in H$\alpha$ flux and H$\alpha$ FWHM. At the highest fluxes, our sample is dominated by BL-AGN. Note that there is a range in wavelength which corresponds to the region between either $Y$ and $J$, $J$ and $H$ or $H$ and $K$, where the atmospheric transmission is extremely low, and thus the apparent drop in the continuum, for sources where the continuum is detected. There are no emission lines in that region, and thus we neglect it for the analysis. Our broadest H$\alpha$ line emitters are BR-64 and BR-60: these indicate high accretion speeds present within the galactic nuclei and/or outflows. BR-64, with $z = 2.197 \pm 0.001$, presents $\mathrm{FWHM}_{\mathrm{H}\alpha} = 11\,500 \pm 700$ km s$^{-1}$, while BR-60, $z = 2.207 \pm 0.001$, has $\mathrm{FWHM}_{\mathrm{H}\alpha} = 10\,500 \pm 1100$ km s$^{-1}$.

**Table 2.** Observing log for the different instruments and grisms used in this study. Each one was capable of observing the H$\alpha$, [N II], [O III] and H$\beta$ lines, with the exception of the blue (*YJH*) grism on SofI, which does not cover [O III] and H$\beta$ for $z \sim 0.81$ targets. The NB$_J$ sample targets H$\alpha$ emitters at $z \sim 0.8$, the NB$_H$ sample targets H$\alpha$ emitters at $z = 1.47$ and the NB$_K$ sample targets H$\alpha$ emitters at $z = 2.23$. Pixel scale is given as observed and in rest frame (R.F.).

| Instrument | Grism | λ coverage (Å, observed) | Sample | No. of sources (H$\alpha$) | Pix. scale (R.F.) (Å pixel$^{-1}$) | Dates observed | Typical seeing (arcsec) |
|---|---|---|---|---|---|---|---|
| WHT/LIRIS | lr_zj | 8870–15 310 | NB$_J$ | 8 | 6 (3.3) | 16–19 Jan 2013 | 0.7 |
| NTT/SofI | Blue | 9500–16 400 | NB$_J$ | 9 | 7 (3.8) | 18–21 Sept 2012 | 0.7 |
| NTT/SofI | Blue | 9500–16 400 | NB$_H$ | 20 | 7 (2.8) | 23–25 Sept 2011 | 0.6 |
| TNG/NICS | *JH* | 11 500–17 500 | NB$_H$ | 8 | 7 (2.8) | 26 Apr 2011, 1–4 Apr 2012 | 1.5 |
| WHT/LIRIS | lr_hk | 13 880–24 190 | NB$_K$ | 8 | 10 (3.1) | 16–19 Jan 2013 | 0.7 |
| NTT/SofI | Red | 15 300–25 200 | NB$_K$ | 6 | 10 (3.1) | 18–21 Sep 2012 | 0.8 |

further jittered with smaller offsets (∼1–3 arcsec) in an ABBAAB sequence for optimal sky subtraction and bad pixel removal. Dome flats and dark and arc frames were taken at the beginning of each night. Telluric stars were observed two to three times per night at the corresponding airmasses and positions to the targets. Telluric stars were reduced by following the same procedure as the science targets, and then used to calibrate the science target spectra. Three targets were acquired directly (centred on the slit directly, as they were bright enough in the continuum). For the other targets, we acquired a nearby bright source and rotated the instrument, so that both the bright source and our science target were on the slit at all times. This not only allowed us to quickly acquire and assure that the science target did not move out of the slit.

Total exposure times varied between 2.7 ks for the most luminous sources and 6 ks for the faintest ones. In our Sep 2011 run, the seeing varied between 0.5 and 0.8 arcsec with a median of 0.6 arcsec. Seeing was similar for the 2012 run, only slightly higher, varying from 0.6 to 0.9 arcsec, but with an average of 0.7 arcsec. During our 2011 run (targeting our NB$_H$ sample), we were able to confirm 20 H$\alpha$ emitters at $z = 1.47$, with a high fraction of broad-line H$\alpha$ emitters. For our 2012 run, targeting our NB$_J$ and NB$_K$ samples, we confirmed nine H$\alpha$ emitters at $z \sim 0.8$ and six at $z = 2.23$.

### 2.2.2 *TNG/NICS: NB$_H$ sample*

We used the NICS instrument (Baffa et al. 2001) with the *JH* grism ($R \sim 500$) and the 1 arcsec slit to observe NB$_H$ candidate line emitters. This instrumental set-up allowed us to probe 11 500–17 500 Å, allowing us to target the rest-frame range ∼4700–7100 Å for sources at $z{\sim}1.47$ (NB$_H$ selected), which were the sole aim of the TNG runs. We used TNG/NICS to observe our targets selected from the COSMOS and Boötes fields on the 2011 April 26, and the 2012 April 1, 2 and 4. During both runs, the seeing was 1–2.5 arcsec, and thus significantly worse than that for e.g. the NTT runs. Dark frames, flats and arcs were obtained at the beginning of the night.

During the 2011 run, we observed two targets, one in COSMOS and one in Boötes, which were acquired directly. We observed one telluric star after observing one of the targets and before moving to the next. During the 2012 run, targets were observed by first acquiring a nearby bright source and then rotating the instrument to align the slit with the bright source and the target. Telluric stars were taken at the beginning, middle and towards the end of each night (so three telluric stars were available for calibration), taken from fields near those under observation at the time. We used individual exposure times of 300 s. In total, using NICS, we were able to confirm eight H$\alpha$ emitters at $z \sim 1.47$ (from our NB$_H$ sample).

#### 2.2.3 *WHT/LIRIS: NB$_J$ and NB$_K$ samples*

We used LIRIS (Manchado et al. 1998) on the WHT to obtain spectra for NB$_J$ and NB$_K$ sources selected from the COSMOS and the UDS fields with the 1 arcsec slit. Over 2013 January 16–19, we obtained spectra of 23 targets in the *HK* (probing 13 880–24 190 Å, rest-frame 4300–7500 Å for sources at $z \sim 2.23$) and ZJ grisms (probing 8800–15 310 Å, rest-frame 4800–8500 Å for sources at $z \sim 0.8$), both yielding a resolution of $R \sim 700$. Individual exposures were 200 s. NB$_K$ targets were observed for up to 8 ks pixel$^{-1}$, while NB$_J$ targets only required up to 2.5 ks pixel$^{-1}$ for similar signal-to-noise (S/N). Three telluric stars were observed per night at the closest possible airmasses and positions to the targets. Darks, flats and arc frames were obtained at the beginning of each night. Across the four nights of observations, weather conditions remained good with only some cirrus on the first night. Seeing was stable between 0.6 and 0.9 arcsec on the first three nights of the run, with a rise to 1.1 arcsec on the final night. The majority of measurements were taken with seeing <1 arcsec. Out of the 23 targets, we confirm 16 H$\alpha$ emitters: 8 at $z = 0.84$ (NB$_J$ sample) and 8 at $z = 2.23$ (NB$_K$ sample).

### 2.3 Data reduction: SofI, LIRIS and NICS

SofI data were reduced using the SofI ESO pipeline version 1.5.4 and ESOREX version 3.9.0 recipes. Briefly, master flat-fields and master arc frames were produced per night, and frames were flattened. Initial wavelength calibrations were produced by matching the master arc frames with catalogued xenon and neon lines. The co-addition recipes corrected for distortion, crosstalk and slit curvature. We then sky-subtracted according to the ABBAAB jitter sequence and average-combined individual reduced frames. While ESOREX provides a reasonable wavelength calibration, we improved upon it by matching ∼50 unblended OH lines. We used a polynomial fit for all our data sets, and determined the coefficients by performing a least-squares fit on OH lines over a wide range of pixels that were detected on the science frames (e.g. Osterbrock et al. 1996). This is consistent with the calibration derived from the arcs, but much more homogeneously spread across the observed spectral range. Standard deviations of residuals to the fits were checked to be random and at the level of ∼4–6 Å, the same order as our pixel scale.

The reduction of NICS and LIRIS data followed the same procedures and steps as for SofI, but the data were reduced with a customized set of PYTHON scripts. All science frames were divided by master flat frames taken on the same night as their observation. Using the offsets of the jittering sequence and the declination of the field, pixel offsets were calculated and the spectra were average-stacked. We applied a clipping of the lowest and highest value pixels within each stack in order to eliminate hot pixels, cosmic rays and other potential artefacts. Some examples of the final 2D spectra are shown in Fig. 1.

### 2.4 Extraction and flux calibration

For spectral extraction, whenever a small distortion across the detector was found, we first corrected for this gradient. We visually inspected each 2D spectrum (e.g. Fig. 1) and extracted the 1D spectrum by summing up the pixels corresponding to ∼1.5–2 arcsec in the spatial direction (we varied this slightly on a source-by-source basis to take into account the seeing variations and any important noisy features), corresponding to ∼15 kpc at all redshifts probed. Some typical examples are shown in Fig. 2. Due to our strategy of acquiring a bright source and then rotating the instrument for the majority of the sources, we almost always have, together with our target, a bright source ($J \sim 13$–15) typically 20–60 arcsec away. These bright sources are also extracted in the same way, over the exact same aperture as our main science target (and any distortions corrected exactly in the same way and checked), and are flux-normalized by telluric spectra taken on the same night, in the same grism as the target spectrum and extracted over the same width.

In order to estimate, and correct for, the light lost out of the slit, we use 2MASS photometry (Skrutskie et al. 2006) and explore the wealth of relatively bright ($J \sim 14$, thus yielding very high S/N for our exposure times) sources which we typically used to acquire our targets and that remained in the slit at all times. By using the known flux density of each of our bright sources (*J* and *H* or *H* and *K*, depending upon grism used), we flux calibrate all our spectra. We note that this process assumes that the target and the bright source are equally well centred in the slit, and of similar apparent angular extent: this is a good assumption for the sources we targeted. We check that the flux calibration that we apply yields emission line fluxes that correlate well (and that have the same normalization within the errors) with the estimates from the narrow-band photometry (see Fig. 3). Differences between NB estimated fluxes and spectroscopic fluxes are fully explained by either errors/uncertainties, redshifts (for some redshifts the filter profile has a lower transmittance, underestimating the flux, which can now be fully checked after determining the redshifts), and due to H$\alpha$ lines which are even broader than the narrow-band filter profile.

## 3 ANALYSIS

### 3.1 Line identification and spectroscopic redshifts

We use both the 1D and 2D spectra in order to first identify the main emission line at the wavelength range covered by the narrow-band filter used to select each source. Out of our 73 targets, we identify a strong emission line in the vast majority of followed-up sources (64 of them, corresponding to a success rate of 88 per cent), with the remaining sources (9) being stars detected with very high S/N continuum and strong features in the NIR which mimic strong emission lines [although all these are easily classed as stars using colour–colour criteria, and thus none are in the Sobral et al. (2013a) samples]. For the sources with an emission line, we produce redshift solutions, starting with identifying the emission line as H$\alpha$, but also assuming that it can be any other strong emission line. We then look for further emission lines, exploring the wide wavelength coverage of all our spectra: we do this simultaneously in the 2D and 1D, and highlight the location of strong OH lines. Finally, after selecting the approximate correct redshift for each source, we fit Gaussian

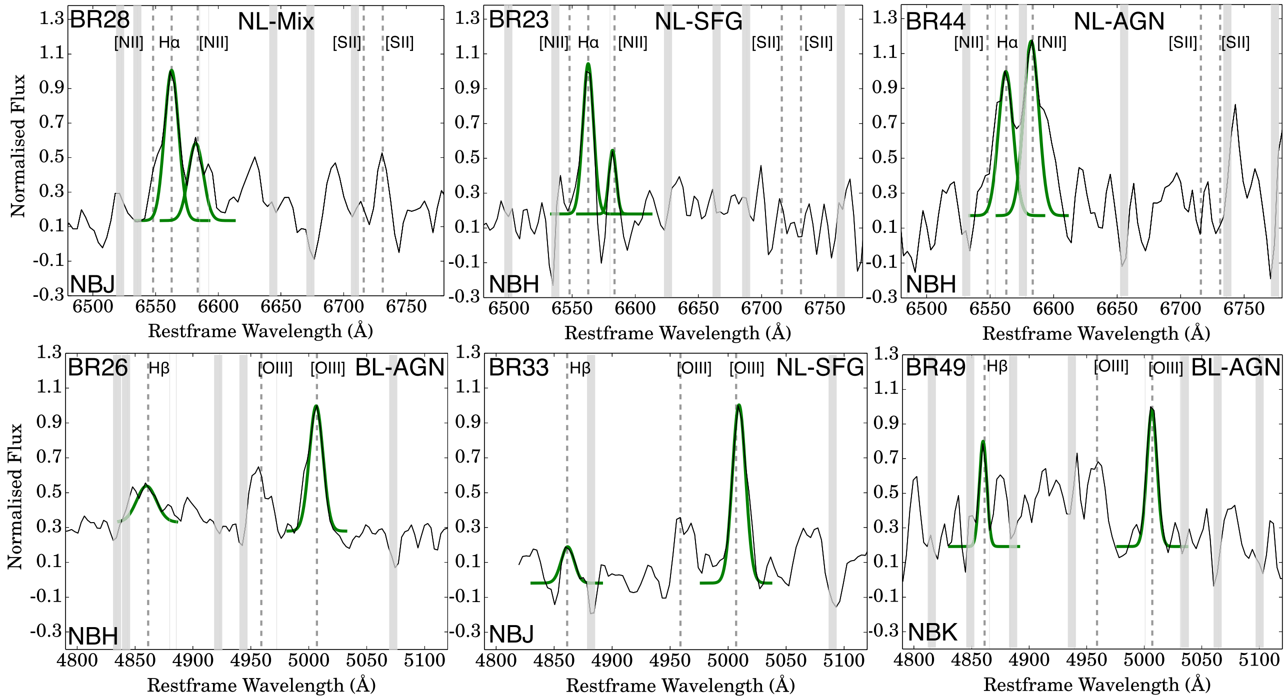

**Figure 2.** A selection of typical spectra showing, for three different sources (top), our coverage which allows us to trace H$\alpha$ and [N II] (and in some cases [S II]) and for another three sources (bottom) our coverage which allows us to trace H$\beta$ and [O III]. We find a variety of sources, but, in general, [O III] is almost always brighter than H$\beta$. Grey vertical lines indicate all OH lines (including weak OH lines) affecting our spectra; green thick lines show our best Gaussian fits for H$\beta$, [O III], H$\alpha$ and [N II].

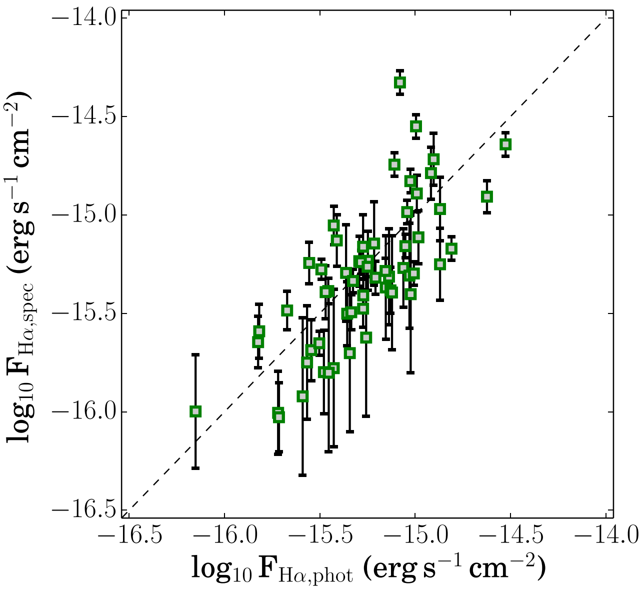

**Figure 3.** A comparison between the spectroscopic H$\alpha$ fluxes and those derived from the narrow-band photometry. The dashed line shows the 1:1 relation. We find good agreement between both, within the uncertainties, and without any strong biases/systematic offset.

profiles to the main emission lines identified, and further refine the redshift and estimate the error on the redshift based on the standard deviation of redshifts obtained using each line individually. We find that out of the 64 emission line sources, 59 (92 per cent) are H$\alpha$ emitters, with the remaining being [O III] emitters and one low-redshift emitter. As Fig. 4 shows, the redshift distribution of H$\alpha$ emitters follows very closely what would be expected given the filter profiles and how efficient they should be at recovering H$\alpha$ (for broad H$\alpha$ the filter profiles are even sensitive to slightly higher and lower redshifts – the filter profiles shown in the figure assume a narrow H$\alpha$ line).

There was no evidence of significant systematic offsets between the redshift determinations from our two strongest lines, H$\alpha$ and [O III] 5007 (see e.g. Fig. 2). For the cases where we found only one line, within the boundaries of the narrow-band filter and not falling on a strong OH line, it was assumed to be H$\alpha$ (provided it was consistent with the lack of other lines). We check that all these single-line sources have photometric redshifts and colours consistent with being H$\alpha$ emitters (e.g. Sobral et al. 2013a). Table 3 presents the full details on the number of sources and the main emission lines detected which will be used to classify the sources. By normalizing at the peak of the H$\alpha$ emission line, we also median stack all the sources. Fig. 5 shows the results.

### 3.2 Line measurements and samples

#### 3.2.1 *Main emission lines*

Our observations covered the wavelength range ∼0.9-2.52 µm in order to probe the rest-frame optical. Our main lines of interest are H$\beta$ (4861 Å), the [O III] doublet (4959, 5007 Å), the [N II] doublet (6548, 6584 Å) and H$\alpha$ (6562.8 Å). For the remaining of the paper, we refer to [O III] 5007 Å and [N II] 6584 Å as [O III] and [N II], respectively. By using the redshift of each source and its error, and the location of each strong OH line, we fit Gaussian profiles to each emission line, after removing the continuum with two linear relations which are calculated independently at the red and at the blue sides of each emission line, by also excluding any nearby

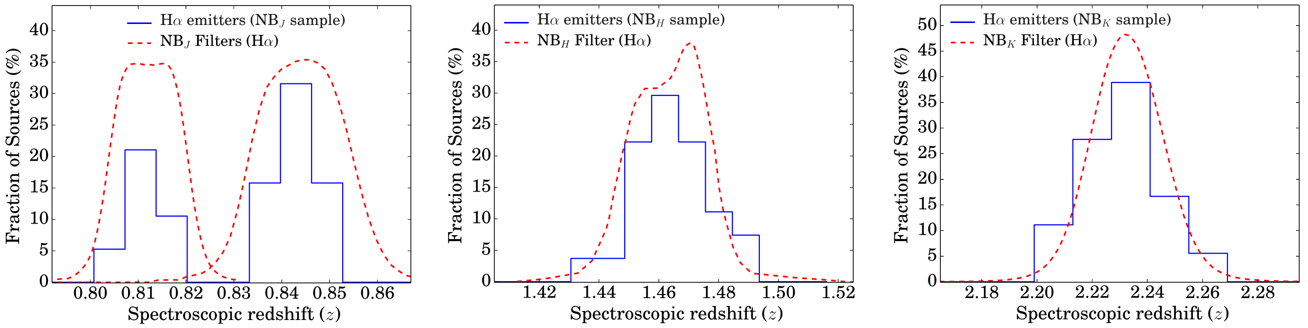

**Figure 4.** Left-to-right: the redshift distributions of our NB$_J$, NB$_H$ and NB$_K$ samples of Hα emitters, respectively. The fraction of sources is simply the number of sources in each bin divided by the full sample at that redshift. In the case of NB$_J$, the relative distribution between the two different narrow-band filters/data sets is simply set by the number of followed-up sources in each data set, as both had an equally high success rate. Overplotted are the narrow-band profiles used for the selection of the samples. This shows that the redshift distribution of each sample follows the filter profile very well.

emission lines and/or strong OH lines. Whenever we fail to detect an emission line with $>2\sigma$, we assign it an upper limit of $2\sigma$. For Hα we fit simultaneously a narrow (typically a few 100 km s$^{-1}$, comparable to the spectral resolution, ∼100–200 km s$^{-1}$) and a broad (typically a few 1000 km s$^{-1}$) Gaussian profile, in an automated way, and without applying any correction for the spectral resolution, as we are mostly interested in distinguishing between broad and narrow lines within the same data set. We also measure line profiles manually, source by source, and check that the results are fully consistent within the errors. Other detected lines in our spectra included Hγ, He II and the [S II] doublet, but only in broad-line AGN (BL-AGN), and these lines are not used in the analysis. Gaussian fits of the emission lines were integrated to obtain line fluxes.

### *3.2.2 Low-S/N sample*

For a fraction of our sources (24 sources; 41 per cent), only one single narrow line is detected, which we assume is Hα. The typical Hα S/N for these 24 sources is ∼2.5–4.5. These sources are found at the lowest fluxes, with an average flux ($4 \times 10^{-16}$ erg s$^{-1}$ cm$^{-2}$) which is ∼2 times lower than the high-S/N sample (Section 3.2.3). It is not possible to further investigate the nature of these apparent narrow-line emitters individually. However, in order to further constrain their nature as a population, we stack the spectra of all these 24 sources. We do not detect [N II], implying a low [N II]/Hα $<$ 0.15, consistent with photoionization by star formation (e.g. Baldwin et al. 1981; Rola, Terlevich & Terlevich 1997; Kewley et al. 2013), and we find [O III]/Hβ ∼5. This probably implies that the majority of the unclassified galaxies are metal-poor SFGs. Thus, while we cannot constrain the nature of these sources individually, we keep these sources for the remaining of the analysis, assuming that the bulk of them are not AGN, in agreement with e.g.

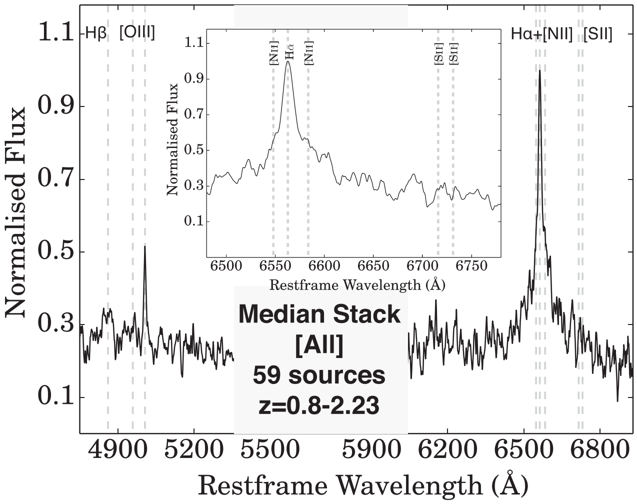

**Figure 5.** The median stack of all 59 sources in our sample by normalizing all sources by the peak of the Hα emission line. This reveals a broad Hα, but that the resulting narrow-line profile dominates. The central region is masking the low-S/N region which results from the very low atmospheric transmission between either $Y$ and $J$, $J$ and $H$ or $H$ and $K$ bands.

**Table 3.** Number of sources in our sample. We first present the full number of sources with spectroscopic redshifts, then the sources with high enough S/N to obtain more information. The numbers of broad- and narrow-line Hα sources are only provided for the high-S/N sources, where one can clearly distinguish between both – all sources with S/N<5 have a narrow Hα emission line, but the S/N is simply not sufficient to see any potential broad component. We then present the number of sources for which we are able to determine line ratios (we label as ‘BPT 4 lines’ the sources for which we can determine both [N II]/Hα and [O III]/Hβ), and those we classify as AGN and SFG. For the unclassified sources, we also show, in parentheses, the number of sources which have high S/N at Hα, but for which it is not possible to classify them, either because they have line ratios that place them between SFGs and AGNs, or, in the case of six sources at $z = 0.8$, because of the lack of blue coverage – the [N II]/Hα ratios of those sources also do not allow to clearly classify any of them as AGN. Unclassified sources are likely to be star-forming dominated.

| Sample | $z_{\rm spec}$ | S/N<5 | S/N>5 | BL Hα | NL Hα | NL [N II]/Hα | BPT 4 lines | SFG | AGN | Unclassified |
|---|---|---|---|---|---|---|---|---|---|---|
| $z = 0.8$ | 17 | 6 | 11 | 1 | 10 | 9 | 4 | 3 | 1 | 13 (7) |
| $z = 1.5$ | 28 | 9 | 19 | 10 | 9 | 9 | 8 | 3 | 14 | 11 (2) |
| $z = 2.2$ | 14 | 9 | 5 | 3 | 2 | 2 | 2 | 1 | 3 | 10 (1) |
| All | 59 | 24 | 35 | 14 | 21 | 20 | 14 | 7 | 18 | 34 (10) |
| Fractions | 100% | 41% | 59% | 24% | 36% | 34% | 24% | 12% | 30% | 58% (17%) |

Stott et al. (2013b) at even lower fluxes, and also with what we find in Section 3.4.

### 3.2.3 *High-S/N sample*

As we are particularly interested in unveiling the nature of the most luminous H$\alpha$ emitters, out of the full sample for which we confirmed and obtained a spectroscopic redshift, we apply an S/N > 5 cut on the H$\alpha$ emission line. This allows us to obtain a sub-sample of 35 luminous H$\alpha$ emitters for which we can further constrain their nature. Table 3 provides information on the full sample and on how many sources have information available for the different lines.

### 3.2.4 *H$\alpha$ FWHM: identifying BL-AGN*

Very broad H$\alpha$ emission with high FWHM (typically $>$1000 km$^{-1}$) can be seen as a clear and robust indication of AGN activity: BL-AGN. Here we use a rest-frame H$\alpha$ FWHM of $>$1000 km s$^{-1}$ to distinguish between what we will henceforth refer to as broad- and narrow-line emitters, which is consistent with the relevant literature (e.g. Stirpe 1990; Ho et al. 1997). Broad-line emitters are hereafter assumed to be AGN, since there are few processes other than gravitational motions close to a central BH that can account for such broadening in a galactic spectrum. For example, strong outflows in massive SFGs at $z \sim 2$ lead to FWHMs of $\sim$450 km s$^{-1}$ (Newman et al. 2012). Much broader emission lines, in excess of 1000 km s$^{-1}$, are seen in central parts of massive galaxies at $z \sim 2$, attributed to AGN activity (Genzel et al. 2014). Starburst-driven galactic winds may be able to drive gas to velocities up to $\sim$3000 km s$^{-1}$ (Heckman 2003), but this would result in highly asymmetric emission line profiles. Although we find tentative evidence for some asymmetry in some of the broader lines (blueshifted), this seems to be on top of a broad, symmetric, BL-AGN H$\alpha$ profile.

We find 14 BL-AGNs out of our sample of 59 H$\alpha$ emitters (24 per cent of the full sample), 1 at $z \sim 0.8$, 10 at $z \sim 1.47$ and 3 at $z = 2.23$. This already reveals that there is a significant fraction of BL-AGN at the highest H$\alpha$ luminosities at $z \sim 0.8$–2.23 and a higher BL-AGN fraction at $z = 1.47$. Among our BL-AGNs, two stand out in particular, as their H$\alpha$ FWHM $> 10^4$ km s$^{-1}$, or about 0.03$c$ (see Fig. 6 for the full distribution of FWHMs). These are BR-60 and BR-64, both at $z \sim 2.2$, shown in Fig. 1.

In Fig. 6, we show the distribution of H$\alpha$ FWHMs for our high-S/N sample and also for sub-samples at each redshift. Narrow-line H$\alpha$ emitters (H$\alpha$ FWHM $\le$ 1000 km s$^{-1}$) dominate the $z \sim 0.8$ distribution, but are still significant contributors to the $z \sim 1.5$ and $z \sim 2.2$ distributions. We note that lower S/N sources not shown in Fig. 6 are consistent with being narrow-line emitters (the stack reveals a narrow H$\alpha$ line $\sim$400 km s$^{-1}$). We further note that we may miss weak BL components, particularly in the lower S/N spectra, and thus BL fractions should conservatively be interpreted as lower limits.

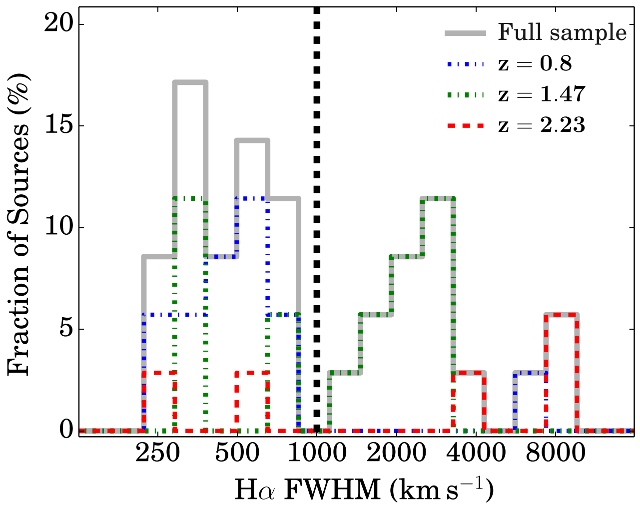

**Figure 6.** The distribution of H$\alpha$ FWHMs for our high-S/N sample (35 sources, see Table 3) in the three redshift ranges we probed (vertical dashed line shows the separation we adopt to differentiate between narrow- and broad-line H$\alpha$ emitters). We find that the typical narrow-line H$\alpha$ emitters have FWHM of $\sim$300–400 km s$^{-1}$ and that these dominate the sample overall, although they are the faintest emitters within our sample – at higher luminosities higher FWHM dominate. The broadest H$\alpha$ lines are found at $z = 2.23$ (see also Fig. 1). The fraction of broad-line emitters is the highest at $z = 1.47$.

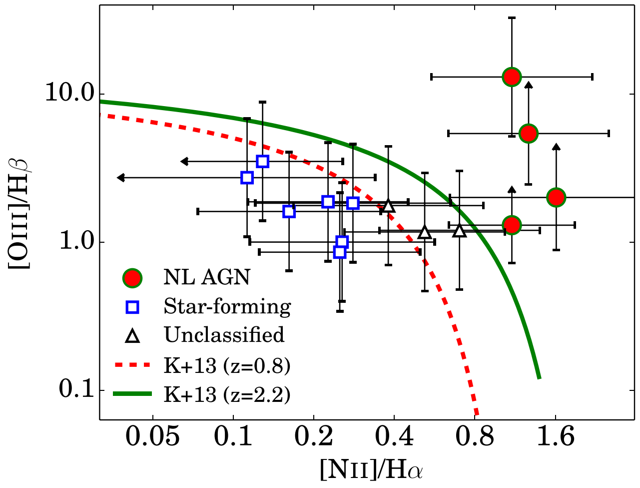

**Figure 7.** SFGs and NL-AGNs can be distinguished from one another, for targets that exhibit narrow-line H$\alpha$ emission, by the line ratios [N II]/H$\alpha$ and [O III]/H$\beta$ (Kewley et al. 2013). We show the line ratios of targets from our NB$_J$, NB$_H$ and NB$_K$ samples. The boundaries between these two populations are shown for the lowest and highest redshifts in the sample from Kewley et al. (2013), and the classification between AGN and star-forming takes into account the redshift. Error bars are the 1$\sigma$ uncertainties in the measurements. Since the purpose here is to distinguish between NL-AGN and NL SF, and because it is not possible to reliably estimate the narrow-line [N II]/H$\alpha$ ratio for the BL-AGN (due to resolution), we do not show the 14 BL-AGNs in our sample.

## 3.3 Distinguishing between NL-AGNs and SFGs

Out of the full sample of 59 H$\alpha$ emitters, we assume that our low-S/N sample (24 sources) are SFGs. For the remaining 35 sources, we already found that 14 are BL-AGN. We now attempt to classify the remaining 21 high-S/N sources, which are all narrow-line emitters, as SFGs or narrow-line AGNs (NL-AGNs). This can be done using emission line ratios (e.g. Baldwin et al. 1981; Rola et al. 1997; Kewley et al. 2013). However, the separation between AGN and typical SFGs has been shown to evolve with redshift (see e.g. Shapley et al. 2015), and thus we use the Kewley et al. (2013) parametrization – although we note that such work is currently mostly theoretical, while observations are starting to provide very useful constraints. Fig. 7 illustrates the use of the Kewley et al. (2013) diagnostic for distinguishing the nature of narrow-line emitters. If we do not detect

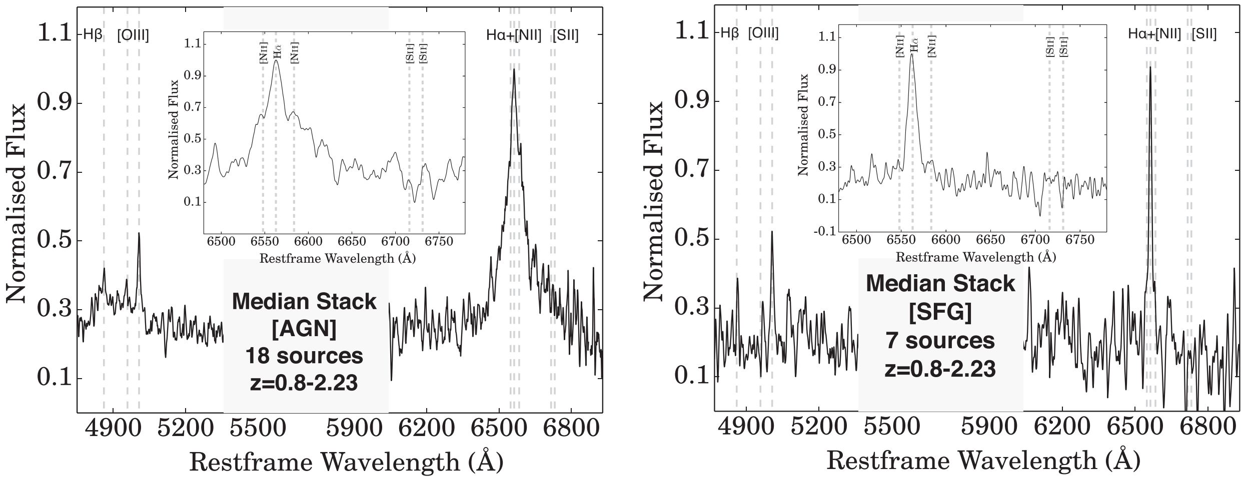

**Figure 8.** Left: the median-stacked spectrum of all AGN in our sample (18 sources used in the stack). The stacks reveal a strong H$\alpha$ line which can only be described fully with a combination of two Gaussian profiles: a dominating profile of ∼4000 km s$^{-1}$ and an even broader profile of ∼10 000 km s$^{-1}$ which also shows some asymmetry suggesting blueshifted emission. These reveal a range in BH masses within our sample, but show that these AGNs are typically very massive, and likely able to drive powerful outflows. We also find broad H$\beta$ in the stack. Right: the median stack for SFGs (seven sources used in the stack), showing strong H$\alpha$, very weak [N II] detections and detections of [O III] and H$\beta$ fully consistent with typical SFGs. The H$\alpha$ emission line is well fitted with a Gaussian profile and FWHM∼300 km s$^{-1}$. We find an [N II]/H$\alpha$ ratio of 0.05 ± 0.02, implying that the median metallicity of our luminous star-forming H$\alpha$ emitters at $z \sim 0.8$–2.2 is $12 + \log(\mathrm{O/H}) = 8.16 \pm 0.08$. Our limit on the [S II]/H$\alpha$ line ratio also implies a very high ionization potential, again consistent with very low metallicity and very high luminosities. Note that the relatively low S/N H$\beta$ detection is also driven by the H$\beta$ line being strong affected by strong OH lines for the bulk of the sample.

H$\beta$ at more than 2$\sigma$ significance due to being affected by a strong OH line, we use the measured limit (three sources, all AGN), but show those as lower limits. In two (2) cases [N II] is below 2$\sigma$. For those we assign the 2$\sigma$ limit as the [N II] flux (but we also plot those as upper limits), and those are the sources with the lowest [N II]/H$\alpha$ in our sample (∼0.1) and are clearly star-forming. Table 3 provides the full information regarding the availability of each of the line ratios, the samples and the results in the classification of sources. We also median stack all sources, after normalizing them to peak H$\alpha$ emission, that we classify as AGN and all the sources we classify as SFGs using the BPT: we show the stacks in Fig. 8.

### 3.4 Lower luminosity H$\alpha$ emitters

In order to estimate the AGN fraction among lower luminosity/more typical H$\alpha$ emitters, and compare with our luminous H$\alpha$ emitters, we explore the general HiZELS sample (Sobral et al. 2013a), which allows us to probe the same redshift ranges as in this study, with the same selection. We use the results from Stott et al. (2013b) that followed up a sample of typical H$\alpha$ emitters from Sobral et al. (2013a) with FMOS/Subaru, finding an AGN fraction of about ∼11 per cent. Within the uncertainties, more typical H$\alpha$ emitters (with lower luminosities) have a much lower AGN fraction than those studied in this paper. This is in good agreement with Garn et al. (2010).

We also use the results from Calhau et al. (2015) for more details on AGN activity for more typical H$\alpha$ emitters within the HiZELS data set. Briefly, deep *Spitzer*/IRAC data are used to search for red colours beyond ∼ 1.6 µm rest frame. A clearly red colour indicates the presence of hot dust and of an AGN, while typical SFGs reveal a blue colour beyond 1.6 µm rest frame.

For $z = 0.8$, we use [3.6]−[4.5] in order to identify AGN, while for $z = 1.47$ we use [4.5]−[5.8] and use [5.8]−[8.0] for $z = 2.23$. Specifically, we use the colour selections [3.6]−[4.5] > 0.0 for $z = 0.8$, [4.5]−[5.8] > 0.15 for $z = 1.47$ and [5.8]−[8.0] > 0.3 for $z = 2.23$. These cuts take into account the distribution of sources and the increase in the scatter of the colour distributions, but are also motivated to select *Chandra* and Very Large Array detections, indicative of AGN activity. This results in a 10 ± 5 per cent AGN fraction at $z = 0.8$, 16 ± 5 per cent at $z = 1.47$ and 15 ± 4 per cent at $z = 2.23$ consistent with little to no evolution, particularly as the samples at higher redshift probe higher H$\alpha$ luminosities.

Overall, the results clearly show that at $z \sim 0.8$–2.23, the AGN fraction of low-luminosity H$\alpha$ emitters ($\leq L^*_{\mathrm{H}\alpha}$) is at a level of ∼10–15 per cent (and certainly below 20 per cent), much lower than that of much higher luminosity H$\alpha$ emitters. We also do not find any significant evidence for redshift evolution.

## 4 RESULTS AND DISCUSSION

For our full sample of 59 H$\alpha$ emitters, we have 24 low-S/N sources, which we are unable to classify, but that are likely star formation dominated. For the remaining 35 sources (the high-S/N sample), we find 14 BL-AGNs, 4 NL-AGNs (thus, 18 AGNs), 7 SFGs and 3 sources which are unclassified. We thus find an AGN fraction of ∼30 per cent among the full sample of 59 H$\alpha$ emitters (see Table 3), and an ∼50 per cent AGN fraction among the high-S/N sample.

### 4.1 BL H$\alpha$ emitters: number densities and BH masses

Using the measured H$\alpha$ FWHMs, H$\alpha$ luminosities and equation 9 from Greene & Ho (2005), we may obtain an estimate of the BH masses of the AGNs in our sample. The average BH mass across all AGNs in our survey is $\sim 10^{8\pm1}$ M$_\odot$, with a relatively high standard deviation mainly coming from larger-than-average masses of the broadest BL-AGNs in the NB$_K$ ($\sim 10^9$ M$_\odot$; see Fig. 1) sample. We note that the estimation of BH masses from line widths is only valid for the cases where we can see the BL region, and thus we restrict our analysis to those. This is because the estimate is based on simple circular motion arguments, thus the need to estimate velocity and radius. We compare our measurements with Heckman & Best

(2014), to find that many of our BL-AGN are relatively ‘normal’ AGN (Heckman & Best 2014), with masses of a few times $10^7$ M$_\odot$, although two of our BL-AGN reach masses more typical of quasars at $z \sim 2$ (e.g. McLure & Dunlop 2004) with $10^9$ M$_\odot$.

Over all redshifts, we find that the volume density of BL-AGN among luminous H$\alpha$ emitters (for volumes where we are spectroscopically complete, thus we do not apply any correction for incompleteness) is $5.7 \pm 1.5 \times 10^{-6}$ Mpc$^{-3}$ ($3 \pm 3 \times 10^{-6}$, $9 \pm 3 \times 10^{-6}$ and $3 \pm 2 \times 10^{-6}$ Mpc$^{-3}$ at $z = 0.8$, 1.47 and 2.23, respectively). Our results are therefore consistent with a constant volume density of BL-AGN at the peak of AGN and star formation activity, of roughly $\sim 6 \times 10^{-6}$ Mpc$^{-3}$, but with a potential peak at $z \sim 1.5$. These number densities are roughly consistent with the number density of massive BL-AGN (e.g. McLure & Dunlop 2004), given the estimates of BH masses for our BL-AGN: $\sim 10^{-6}$–$10^{-5}$ Mpc$^{-3}$. As mentioned in Section 3.2.4, we note that we may miss weak BL components, particularly in the lower S/N spectra, and thus our number density of massive BL-AGN should conservatively be interpreted as lower limits. While our sample of BL-AGN is too small to further split it per redshift, our findings are consistent with a decrease in the BL-AGN fraction for fixed H$\alpha$ luminosity, with increasing redshift.

**Table 4.** Best-fitting linear relation as a function of different quantities/properties (all in log$_{10}$ form): H$\alpha$ observed flux, H$\alpha$ observed luminosity and $L_{\mathrm{H}\alpha}/L^*_{\mathrm{H}\alpha}(z)$. We provide parameters $A$ and $B$ for each property/quantity, $x$ (AGN fraction= $Ax + B$), including the 1$\sigma$ error for each parameter when fitting both simultaneously.

| Property – sample | $A$ | $B$ |
|---|---|---|
| H$\alpha$ flux (log$_{10}$) – All | $0.47 \pm 0.13$ | $7.5 \pm 2.0$ |
| H$\alpha$ flux (log$_{10}$) – S/N >5 | $0.81 \pm 0.27$ | $12.9 \pm 4.1$ |
| H$\alpha$ luminosity (log$_{10}$) – All | $0.38 \pm 0.09$ | $-15.8 \pm 3.6$ |
| H$\alpha$ luminosity (log$_{10}$) – S/N >5 | $0.66 \pm 0.19$ | $-27.6 \pm 8.2$ |
| $L_{\mathrm{H}\alpha}/L^*_{\mathrm{H}\alpha}(z)$ (log$_{10}$) – All | $0.54 \pm 0.13$ | $-0.04 \pm 0.06$ |
| $L_{\mathrm{H}\alpha}/L^*_{\mathrm{H}\alpha}(z)$ (log$_{10}$) – S/N >5 | $0.75 \pm 0.19$ | $0.06 \pm 0.10$ |

## 4.2 Evolution of AGN fraction with H$\alpha$ flux, luminosity, cosmic-normalized luminosity and redshift

Here we investigate how the fraction of AGN among H$\alpha$ emitters varies with H$\alpha$ flux, luminosity and $L_{\mathrm{H}\alpha}/L^*_{\mathrm{H}\alpha}(z)$, for our full sample, and when we restrict the sample to only sources we can individually classify. We also provide the best linear fit for each of the relations we find (see Table 4). Results for each redshift are presented in Table 5.

As the left-hand panel of Fig. 9 shows, the AGN fraction rises significantly with increasing observed H$\alpha$ flux. This is seen both when we use the full sample and the sample of classified sources only. This is mostly driven by the bright BL-AGNs which, even at higher redshift ($z \sim 2.2$, 1.47), are able to produce observable fluxes which are still much higher than more typical SFGs at $z \sim 0.8$.

We also find a strong correlation between the AGN fraction and H$\alpha$ luminosity, shown in the middle panel of Fig. 9. However, given that the typical H$\alpha$ luminosity is strongly increasing with look-back

**Table 5.** Results for our different samples. Note that the NB$_J$ sample is selected with two different narrow-band filters (see Fig. 4). $\phi$ (BL-AGN) is the number density of BL-AGN. Note that the samples at $z \sim 1.5$ and $z \sim 2.2$ present a much larger AGN fraction and a much larger BL-AGN fraction, but they also reach much higher luminosities and higher $L^*$.

| Sample | $\bar{z}_{\mathrm{spec}}$ | Look-back time (Gyr) | $f_{\mathrm{BL\text{-}AGN}}$ | $\phi$ (BL-AGN) ($\times 10^{-6}$ Mpc$^{-3}$) | $f_{\mathrm{AGN}}$ | Obs. log $L_{\mathrm{H}_\alpha}$ [log (erg s$^{-1}$)] | $L_{\mathrm{H}\alpha}/L^*(z)$ [$L^*(z)$] |
|---|---|---|---|---|---|---|---|
| NB$_J$ | 0.84 | 7.0 | $6 \pm 6$ | $3 \pm 3$ | $6 \pm 6$ | $42.34 \pm 0.18$ | 1.2–6 |
| NB$_H$ | 1.47 | 9.2 | $36 \pm 13$ | $9 \pm 3$ | $50 \pm 16$ | $43.01 \pm 0.35$ | 1.9–50 |
| NB$_K$ | 2.23 | 10.6 | $21 \pm 14$ | $3 \pm 2$ | $21 \pm 14$ | $43.16 \pm 0.32$ | 1.0–23 |

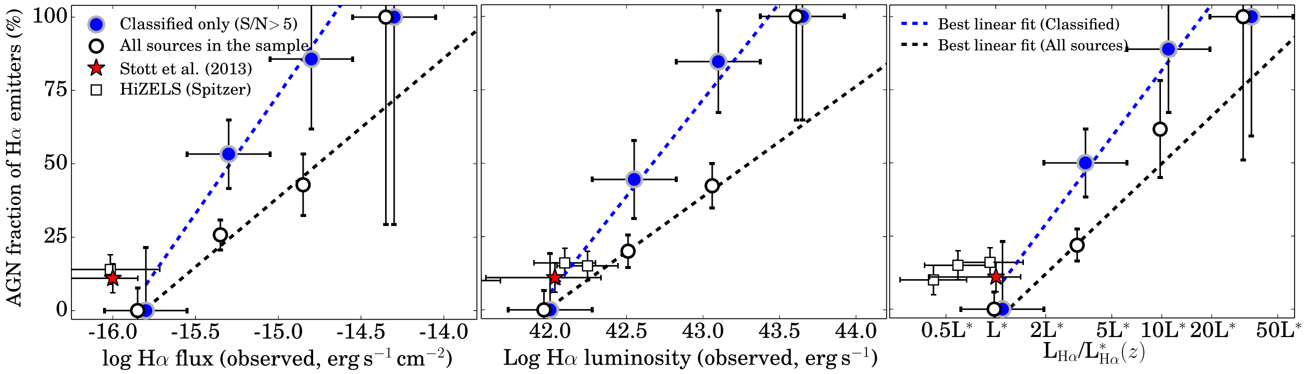

**Figure 9.** Left: the fraction of AGN as a function of H$\alpha$ observed flux when considering only directly classified sources and for the full sample (including the lower S/N sources; bins shifted by $-0.05$ so they do not overlap). We also show the best linear fits (see Table 4). This shows a strong increase in the fraction of AGN for higher fluxes, dominated by the rise of the fraction of BL-AGN. However, high luminosities at high redshift will be observed as lower observed fluxes. Middle: the fraction of AGN as a function of H$\alpha$ luminosity. We find that the AGN fraction is higher at the highest H$\alpha$ luminosities. However, as shown in Sobral et al. (2013a), the typical luminosity of H$\alpha$ emitters evolves significantly with cosmic time. Right: by taking into account the evolution of $L^*$, we recover a strong relation between the location within the H$\alpha$ luminosity at each redshift and the AGN fraction. This shows that while around $L^*$ and lower H$\alpha$ luminosities only a minor fraction of H$\alpha$-selected sources are AGN, the fraction rises steeply for higher luminosities. The Stott et al. (2013b) study observed and characterized lower luminosity HiZELS sources shown here for comparison, as it extends our results to lower fluxes and lower values. For comparison, we show the AGN fraction estimated for the HiZELS sample, as detailed in Section 3.4. We also show the best linear fits and table presents the best-fitting coefficients and errors (1$\sigma$).

time/redshift, we also look for a potential correlation between the AGN fraction and the cosmic-normalized Hα luminosity, which is simply $L_{\mathrm{H}\alpha}$ at a redshift $z$ divided by $L^*_{\mathrm{H}\alpha}(z)$ by using the results presented in Sobral et al. (2013a). Similar uses of this normalized quantity can be seen in e.g. Sobral et al. (2010) and Stott et al. (2013a). As the right-hand panel of Fig. 9 clearly shows, there is a strong correlation between AGN fraction and how luminous an Hα emitter is relative to the typical Hα luminosity ($L^*_{\mathrm{H}\alpha}$) at its cosmic time. The AGN fraction measured by Stott et al. (2013b), and those by Garn et al. (2010), of much more typical Hα emitters from the same survey, also fully agrees with this trend. Our further investigation also shows that at $L^*$ and below, at all the redshifts probed, the AGN fraction is ∼10–15 per cent. However, as our results show, the AGN fraction rises with increasing $L/L^*_{\mathrm{H}\alpha}$, becoming ∼25 per cent by $\sim 2L^*_{\mathrm{H}\alpha}$, 50 per cent by $\sim 5L^*_{\mathrm{H}\alpha}$ and becoming essentially 100 per cent by $\sim 50L^*_{\mathrm{H}\alpha}$, the most luminous sources in our survey.

We test the statistical significance of the trends that we observe, particularly to evaluate which is the best predictor of the AGN fraction: Hα flux, luminosity or $L/L^*_{\mathrm{H}\alpha}(z)$. We use our binned data to find that all trends (with flux, luminosity and $L/L^*_{\mathrm{H}\alpha}(z)$) are significant at $>3\sigma$ on their own (comparing to no relation, i.e. a constant), considering only the classified sources (and considering all sources in parentheses); $3.3(5.5)\sigma$, $3.1(5.1)\sigma$ and $4.6(6.4)\sigma$, respectively, for Hα flux, luminosity and $L/L^*_{\mathrm{H}\alpha}$ – revealing that the AGN fraction correlates most strongly with $L/L^*_{\mathrm{H}\alpha}(z)$, for both the classified sources and when using the entire sample. Including the data point from Stott et al. (2013b) increases the significance of the trends by about $1\sigma$, but differences are maintained. We further investigate the significance of the trends we find by binning the data 100 000 times with a range of random bin centres and bin widths within the parameter space that we probe. The results confirm that there is a significant relation between the AGN fraction and Hα flux, luminosity and $L/L^*_{\mathrm{H}\alpha}(z)$, with all fits being at least $5\sigma$ away from no relation. We also find that the correlation is always more significant with $L/L^*_{\mathrm{H}\alpha}(z)$. We therefore conclude that while the three quantities are good predictors of the AGN fraction, for our probed parameter range, $L/L^*_{\mathrm{H}\alpha}(z)$ is the best.

Since we see that the AGN fraction is very high for Hα emitters higher than $L^*$ at all epochs and $L^*$ is evolving very strongly with cosmic time, it is possible that the two are somewhat connected. However, this does not necessarily mean that AGNs are quenching star formation. Indeed, we may just be witnessing that with more gas (and higher gas fractions), there is simply more accretion into the BH (and more stars being formed) that is just driven by the gas supply without the AGN necessarily coupling to the SF (e.g. Mullaney et al. 2012).

Even though our samples at each redshift are not very large, we also investigate if there is any strong evolution of the AGN fraction with redshift. Given that we find that the AGN fraction correlates very strongly with $L/L^*_{\mathrm{H}\alpha}(z)$, we take into account the $L/L^*_{\mathrm{H}\alpha}(z)$ distribution of the samples at the different redshifts ($z = 0.8$, 1.47, 2.23). Our $z = 0.8$ sample probes $L/L^*_{\mathrm{H}\alpha}(z) \sim 1-6$ (average of 3.1), while we probe $L/L^*_{\mathrm{H}\alpha}(z) \sim 1-50$ (average of 8) at $z = 1.47$ and $L/L^*_{\mathrm{H}\alpha}(z) \sim 1-23$ (average of 4) at $z = 2.23$. This would imply, under the scenario of no AGN evolution with redshift, AGN fractions of ∼20, ∼50 and ∼30 per cent at $z = 0.8$, 1.47 and 2.23, respectively, while we find 6 ± 6, 50 ± 16 and 21 ± 14 per cent. Thus, our results are consistent with no significant evolution of the AGN fraction with redshift, although there may be a slight decrease (at $2\sigma$ significance) from $z \sim 1.5$–2.2 to $z = 0.8$. Larger samples at each individual redshifts would be required to further test this.

### 4.3 AGN (de)contamination and an improvement on the accuracy of star-forming history among luminous Hα emitters

By removing AGN from our sample of luminous Hα emitters, we derive the SFR density for such luminous sources and study its evolution. We present our results in Fig. 10 (green circles). We show the full integration of Hα star formation rate density ($\rho_{\mathrm{SFR}}$) against redshift, with our AGN decontaminations applied to the three HiZELS redshift bins from Sobral et al. (2013a). We note that for all cases we use $A_{\mathrm{H}\alpha} = 1$ for dust corrections (see e.g. Sobral et al. 2012, 2013a; Ibar et al. 2013).

We present three different ways of investigating the evolution of the SFR density in Fig. 10. The full integration presents the full SFR density in which the AGN decontamination at the bright end of the Hα LF has little effect. This reveals that even though the highest Hα luminosity samples are significantly affected by AGN, the overall measurement is not affected significantly, because the SFR density at any epoch is dominated by the faintest Hα emitters, for which the AGN fraction is low (∼10–15 per cent at most).

We also present the star formation history when integrating down to roughly the combined Hα luminosity limit of our samples, $L_{\mathrm{H}\alpha} = 10^{42}$ erg s$^{-1}$ (observed, thus $L_{\mathrm{H}\alpha} = 10^{42.4}$ erg s$^{-1}$ after dust correction), before and after removing AGN. Our results reveal that the strong evolution of luminous Hα SFGs across redshift, as $\rho_{\mathrm{SFR}}$ (down to a fixed luminosity limit), increases by a factor of ∼1300 over the range of redshifts shown, attributed to the most strongly star-forming Hα-selected galaxies from $z = 0$ to 2.23. Here the effect of AGN decontamination is much more important. Such rise in the contribution of highly star-forming systems to the total SFR density, and the much stronger evolution with cosmic time, is also seen in extremely star-forming populations such as sub-millimetre galaxies (SMGs) or FIR-selected galaxies at high flux thresholds, e.g. ultraluminous infrared galaxies (ULIRGs; e.g. Smail, Ivison & Blain 1997; Chapman et al. 2005; Caputi et al. 2007; Magnelli et al. 2011, 2013).

Finally, we present the SFR density due to $L_{\mathrm{H}\alpha} > L^*_{\mathrm{H}\alpha}(z)$ SFGs (after removing all AGN). We use our samples for $z = 0.8$–2.23, and also include the results at $z \sim 0.2$ presented in Stroe & Sobral (2015, assuming that the relation between AGN contamination and e.g. $L_{\mathrm{H}\alpha}/L^*_{\mathrm{H}\alpha}(z)$ does not evolve down to $z = 0.2$), which provides a comparable narrow-band survey that successfully probes beyond $L^*$ and overcomes cosmic variance. Integrating down to $L > L^*(z)$ is a much fairer quantification of how much star formation density is occurring in the most star-forming galaxies at each redshift, as it takes into account that the typical Hα luminosity (typical SFR; see e.g. Sobral et al. 2014) of galaxies is increasing with redshift. Once this is computed, the results shown in Fig. 10 clearly reveal a very flat relative contribution of the most star-forming galaxies to the total SFR density, after removing AGN. This contribution is at the level of ∼15 per cent, independent of cosmic time. We note that such contribution matches very well the contribution of mergers to the total SFR density (e.g. Sobral et al. 2009; Stott et al. 2013a). Mergers have been found to dominate the Hα LF above $L^*_{\mathrm{H}\alpha}(z)$, at least at $z = 0.8$ (see Sobral et al. 2009), and our results are consistent with this being the case at least up to $z \sim 2.23$.

## 5 CONCLUSIONS

We have investigated the nature and evolution of the most luminous Hα emitters across the peak of the star formation and AGN activity in the Universe ($z = 0.8$–2.23) by conducting spectroscopic observations with NTT/SofI, WHT/LIRIS and TNG/NICS. We selected

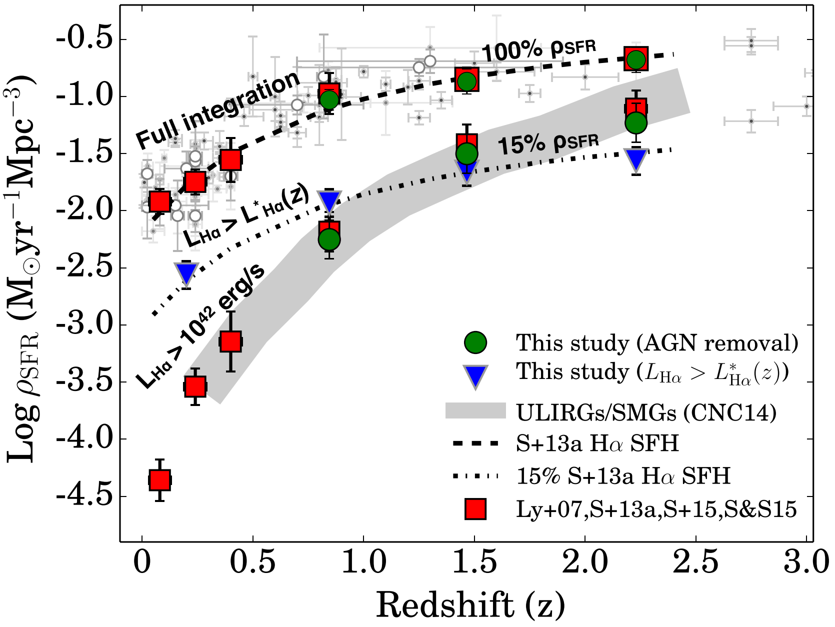

**Figure 10.** The SFR density with increasing redshift. Our AGN-decontaminated SFR densities as applied to Sobral et al. (2013a) are shown (green circles), and compared to the simpler fixed AGN contamination used in that paper of 10 per cent for $z < 1$ (Garn et al. 2010) and 15 per cent for $z > 1$ (red squares). The background data points for the full integration are from the literature (e.g. Hopkins & Beacom 2006, and references therein). While AGN decontamination does not change the total integration of the $\rho_{\rm SFR}$ history noticeably (due to the dominant role of the $L_{\rm H\alpha} < L^*_{\rm H\alpha}$ sources at all redshifts), it becomes much more important for the most luminous sources, due to the higher AGN fractions at high luminosities. We find that the most luminous sources ($L_{\rm H\alpha} > L^*_{\rm H\alpha}$) exhibit an evolution in $\rho_{\rm SFR}$ that changes by ∼3 orders of magnitude over the redshifts shown when integrating down to $L_{\rm H\alpha} = 10^{42}$ erg s$^{-1}$ (observed, thus $L_{\rm H\alpha} = 10^{42.4}$ erg s$^{-1}$ after dust corrected), which corresponds to $L_{\rm H\alpha} > 3.4\,L^*_{\rm H\alpha}(z = 0)$, but to only $0.34L^*$ at $z = 2.23$ (thus one is integrating further down the LF as a function of increasing redshift). Such evolution is very well matched with that found for 'ULIRGs' (defined in respect to $z = 0$ with a fixed luminosity cut) and SMGs (CNC14: Casey, Narayanan & Cooray 2014). However, if we take into account the evolution of $L^*_{\rm H\alpha}(z)$, and integrate the Hα LF only above $L^*(z)$ at each redshift, and remove all AGNs, we find that the fraction contribution of the extreme Hα emitters is surprisingly constant across cosmic time, approximately ∼15 per cent. This reveals how it is misleading to integrate down to a fixed limit when LFs are evolving very strongly in luminosity (thus the typical luminosity is changing).

59 luminous Hα emitters over three redshift slices ($>L^*_{\rm H\alpha}$ at each epoch) at $z \sim 0.8$, 1.5 and 2.2 from the HiZELS and CF-HiZELS surveys and obtained NIR spectra of these sources. By analysing their NIR spectra, we have unveiled their nature. Our main results are as follows.

(i) We find that, overall, 30 ± 8 per cent of luminous Hα emitters are AGN without any strong evolution with $z$ within the errors and particularly when taking into account the different Hα luminosities probed). We find that 80 ± 30 per cent of the AGN among luminous Hα emitters are BL-AGNs.

(ii) Our BL-AGNs have BH masses which span a relatively large range: from relatively typical BH masses of a few $10^7$ $\rm M_\odot$ to more quasar like BH masses at $z \sim 2$ ($\sim 10^9$ $\rm M_\odot$). These completely dominate the most luminous end of the Hα LF.

(iii) The AGN fraction and the fraction of BL-AGN among luminous Hα emitters increase strongly with Hα flux, with Hα luminosity and with $L/L^*(z)$ at all redshifts, with $L/L^*(z)$ being the strongest predictor of the AGN fraction and matching well the lower AGN fractions found for lower luminosity Hα emitters.

(iv) While we find that $L^*_{\rm H\alpha}$ and lower luminosity Hα emitters are dominated by SFGs, the most luminous Hα emitters becoming increasingly AGN dominated at all cosmic epochs probed ($L > 10L^*_{\rm H\alpha}(z)$) at any cosmic time are essentially all (∼100 per cent) BL-AGN.

(v) Using our AGN-decontaminated sample of SFGs, we also derive the star formation history for the most luminous Hα emitters since $z \sim 2.23$. Our results reveal a factor of ∼1300 evolution in the SFR density attributed to the most strongly star-forming Hα-selected galaxies from $z = 0$ to 2.23. However, by integrating down to the evolving $L^*_{\rm H\alpha}(z)$, and classifying those as the most star-forming galaxies at any specific cosmic time, we show that the most star-forming galaxies at all redshifts up to $z \sim 2.23$ have a constant contribution to the total SFR density of about 15 per cent.

Our results are important in order to understand the nature and evolution of luminous Hα emitters. We also find that the more luminous in Hα a source is, the more likely it is to be an AGN, and the more likely it is to be a BL-AGN, indicating that for the highest luminosities at any cosmic epoch, AGNs are the main powering mechanism. However, once one looks at more typical sources, the AGN fraction quickly reduces to ∼10–15 per cent.

## ACKNOWLEDGEMENTS

The authors would like to thank the anonymous reviewer for the many helpful comments and suggestions which greatly improved the clarity and quality of this work. DS and SAK acknowledge financial support from the Netherlands Organisation for Scientific research (NWO) through a Veni fellowship. DS also acknowledges funding from FCT through an FCT Investigator Starting Grant and Start-up Grant (IF/01154/2012/CP0189/CT0010) and from FCT grant PEst-OE/FIS/UI2751/2014. Part of this project was undertaken during the inaugural Leiden/ESA Astrophysics Program for Summer Students (LEAPS). IRS acknowledges support from STFC (ST/L00075X/1), the ERC Advanced Investigator programme DUSTYGAL 321334 and a Royal Society/Wolfson merit award. CH acknowledges support from STFC. Based on observations made with ESO Telescopes at the La Silla Paranal Observatory under programme ID 087.A-0337 and ID 089.A-0965. Also based on data from the Telescopio Nazionale Galileo, with time awarded through OPTICON programmes 2011A/026 and 2012A020 and the William Herschel Telescope under programme W12BN007. The William Herschel Telescope is operated on the island of La Palma by the Isaac Newton Group in the Spanish Observatorio del Roque de los Muchachos of the Instituto de Astrofisica de Canarias. The authors wish to thank all the help given by the telescope staff from all the observatories used in this study: ESO staff in La Silla, and the TNG and WHT staff in La Palma. This publication makes use of data products from the Two Micron All-Sky Survey, which is a joint project of the University of Massachusetts and the Infrared Processing and Analysis Center/California Institute of Technology, funded by the National Aeronautics and Space Administration and the National Science Foundation.

## REFERENCES

Ackermann M. et al., 2011, ApJ, 743, 171
Aird J. et al., 2010, MNRAS, 401, 2531
An F. X. et al., 2014, ApJ, 784, 152
Baffa C. et al., 2001, A&A, 378, 722
Baldwin J. A., Phillips M. M., Terlevich R., 1981, PASP, 93, 5
Best P. et al., 2013, Astrophysics and Space Science Proc. Vol. 37, Thirty Years of Astronomical Discovery with UKIRT. Springer, Dordrecht, p. 235
Brand K. et al., 2006, ApJ, 641, 140
Brandt W. N., Alexander D. M., 2015, A&AR, 23, 1
Brinchmann J., Charlot S., White S. D. M., Tremonti C., Kauffmann G., Heckman T., Brinkmann J., 2004, MNRAS, 351, 1151
Calhau J. et al., 2015, MNRAS, submitted
Caputi K. I. et al., 2007, ApJ, 660, 97
Casey C. M., Narayanan D., Cooray A., 2014, Phys. Rep., 541, 45
Chapman S. C., Blain A. W., Smail I., Ivison R. J., 2005, ApJ, 622, 772
Colbert J. W. et al., 2013, ApJ, 779, 34
Darvish B., Sobral D., Mobasher B., Scoville N. Z., Best P., Sales L. V., Smail I., 2014, ApJ, 796, 51
Domínguez A. et al., 2013, ApJ, 763, 145
Drake A. B. et al., 2015, MNRAS, 454, 2015
Fu H. et al., 2010, ApJ, 722, 653
Fumagalli M. et al., 2012, ApJ, 757, L22
Garn T. et al., 2010, MNRAS, 402, 2017
Geach J. E., Smail I., Best P. N., Kurk J., Casali M., Ivison R. J., Coppin K., 2008, MNRAS, 388, 1473
Geach J. E., Sobral D., Hickox R. C., Wake D. A., Smail I., Best P. N., Baugh C. M., Stott J. P., 2012, MNRAS, 426, 679
Genzel R. et al., 2014, ApJ, 796, 7
Greene J. E., Ho L. C., 2005, ApJ, 630, 122
Hayes M., Schaerer D., Östlin G., 2010, A&A, 509, L5
Heckman T. M., 2003, Rev. Mex. Astron. Astrofis. Ser. Conf., 17, 47
Heckman T. M., Best P. N., 2014, ARA&A, 52, 589
Ho L. C., Filippenko A. V., Sargent W. L. W., Peng C. Y., 1997, ApJS, 112, 391
Hopkins A. M., Beacom J. F., 2006, ApJ, 651, 142
Ibar E. et al., 2013, MNRAS, 434, 3218
Karim A. et al., 2011, ApJ, 730, 61
Kennicutt R. C., Jr, 1998, ARA&A, 36, 189
Kewley L. J., Maier C., Yabe K., Ohta K., Akiyama M., Dopita M. A., Yuan T., 2013, ApJ, 774, L10
Khostovan A. A., Sobral D., Mobasher B., Best P. N., Smail I., Stott J. P., Hemmati S., Nayyeri H., 2015, MNRAS, 452, 3948
Kirkpatrick A. et al., 2012, ApJ, 759, 139
Koyama Y. et al., 2013, MNRAS, 434, 423
Kriek M. et al., 2015, ApJS, 218, 15
Kurk J. D., Pentericci L., Overzier R. A., Röttgering H. J. A., Miley G. K., 2004, A&A, 428, 817
Lacy M. et al., 2004, ApJS, 154, 166
Lacy M. et al., 2007, AJ, 133, 186
LaMassa S. M., Heckman T. M., Ptak A., Schiminovich D., O'Dowd M., Bertincourt B., 2012, ApJ, 758, 1
Lawrence A. et al., 2012, VizieR Online Data Catalog, 2314, 0
Lee J. C. et al., 2012, PASP, 124, 782
Lilly S. J., Le Fevre O., Hammer F., Crampton D., 1996, ApJ, 460, L1
Livermore R. C. et al., 2012, MNRAS, 427, 688
McLean I. S., Steidel C. C., Matthews K., Epps H., Adkins S. M., 2008. Proc. SPIE, 7014, 70142Z
McLure R. J., Dunlop J. S., 2004, MNRAS, 352, 1390
Magnelli B., Elbaz D., Chary R. R., Dickinson M., Le Borgne D., Frayer D. T., Willmer C. N. A., 2011, A&A, 528, A35
Magnelli B. et al., 2013, A&A, 553, A132
Manchado A. et al., 1998, Proc. SPIE, 3354, 448
Matthee J. J. A. et al., 2014, MNRAS, 440, 2375
Moorwood A., Cuby J.-G., Lidman C., 1998, The Messenger, 91, 9
Mullaney J. R. et al., 2012, ApJ, 753, L30
Newman S. F. et al., 2012, ApJ, 761, 43
Obrić M. et al., 2006, MNRAS, 370, 1677
Osterbrock D. E., Fulbright J. P., Martel A. R., Keane M. J., Trager S. C., Basri G., 1996, PASP, 108, 277
Price S. H. et al., 2014, ApJ, 788, 86
Reddy N. A., Steidel C. C., Pettini M., Adelberger K. L., Shapley A. E., Erb D. K., Dickinson M., 2008, ApJS, 175, 48
Rola C. S., Terlevich E., Terlevich R. J., 1997, MNRAS, 289, 419
Schenker M. A., Ellis R. S., Konidaris N. P., Stark D. P., 2013, ApJ, 777, 67
Scoville N. et al., 2007, ApJS, 172, 1
Shapley A. E. et al., 2015, ApJ, 801, 88
Sharples R. et al., 2006, New Astron. Rev., 50, 370
Skrutskie M. F. et al., 2006, AJ, 131, 1163
Smail I., Ivison R. J., Blain A. W., 1997, ApJ, 490, L5
Smolčić V. et al., 2006, MNRAS, 371, 121
Sobral D. et al., 2009, MNRAS, 398, 75
Sobral D., Best P. N., Geach J. E., Smail I., Cirasuolo M., Garn T., Dalton G. B., Kurk J., 2010, MNRAS, 404, 1551
Sobral D., Best P. N., Matsuda Y., Smail I., Geach J. E., Cirasuolo M., 2012, MNRAS, 420, 1926
Sobral D., Smail I., Best P. N., Geach J. E., Matsuda Y., Stott J. P., Cirasuolo M., Kurk J., 2013a, MNRAS, 428, 1128
Sobral D. et al., 2013b, MNRAS, 779, 139
Sobral D., Best P. N., Smail I., Mobasher B., Stott J., Nisbet D., 2014, MNRAS, 437, 3516
Sobral D. et al., 2015, MNRAS, 451, 2303
Sobral D., Stroe A., Dawson W. A., Wittman D., Jee M. J., Röttgering H., van Weeren R. J., Brüggen M., 2015, MNRAS, 450, 630
Stern D. et al., 2012, ApJ, 753, 30
Stirpe G. M., 1990, A&A, 85, 1049
Stott J. P., Sobral D., Smail I., Bower R., Best P. N., Geach J. E., 2013a, MNRAS, 430, 1158
Stott J. P. et al., 2013b, MNRAS, 436, 1130
Stott J. P. et al., 2014, MNRAS, 443, 2695
Stroe A., Sobral D., 2015, MNRAS, 453, 242
Swinbank A. M., Sobral D., Smail I., Geach J. E., Best P. N., McCarthy I. G., Crain R. A., Theuns T., 2012, MNRAS, 426, 935
Swinbank A. M. et al., 2014, MNRAS, 438, 1267
Tadaki K.-i., Kodama T., Tanaka I., Hayashi M., Koyama Y., Shimakawa R., 2013, ApJ, 778, 114
Trump J. R. et al., 2013, ApJ, 763, L6
Ueda Y., Akiyama M., Hasinger G., Miyaji T., Watson M. G., 2014, ApJ, 786, 104
Wolf C., Wisotzki L., Borch A., Dye S., Kleinheinrich M., Meisenheimer K., 2003, A&A, 408, 499
Wuyts E. et al., 2014, ApJ, 789, L40

## SUPPORTING INFORMATION

Additional Supporting Information may be found in the online version of this article:

**Table A1.** Example entries from the catalogue of 59 sources. (http://www.mnras.oxfordjournals.org/lookup/suppl/doi:10.1093/mnras/stw022/-/DC1).

## APPENDIX

**Table A1.** Example entries from the catalogue of 59 sources. The full catalogue is available online.

| ID | RA (J2000) | Dec. (J2000) | $z_{\rm spec}$ | log $L_{\rm H\alpha}$ (erg s$^{-1}$) | $L_{\rm H\alpha}/L^*_{\rm H\alpha}$ | FWHM H$\alpha$ (km s$^{-1}$) | [N II]/H$\alpha$ log | [O III]/H$\beta$ log | Class | Instrument |
|---|---|---|---|---|---|---|---|---|---|---|
| BR-03 | 02:19:08.8 | −04:40:35.7 | 1.4845 ± 0.0005 | 42.46 | 2.1 | 430 ± 91 | − 0.89 ± 0.42 | 0.54 ± 0.30 | SFG | SofI |
| BR-04 | 02:17:08.7 | −04:57:41.5 | 1.4394 ± 0.0009 | 42.65 | 3.4 | 2225 ± 168 | − 0.94 ± 0.42 | − 0.06 ± 0.35 | BL-AGN | SofI |
| BR-05 | 02:17:37.2 | −04:46:12.3 | 1.4621 ± 0.0002 | 42.68 | 3.5 | 979 ± 167 | − 0.55 ± 0.44 | 0.26 ± 0.36 | SFG | SofI |
| – | – | – | – | – | – | – | – | – | – | |

This paper has been typeset from a TEX/LATEX file prepared by the author.